Nanoscale

PAPER

View Article Online
View Journal

Cite this: DOI: 10.1039/d5nr05105c

Persistent, broad-spectrum antimicrobial activity of multi-metal surface phase-modified ceria nanozymes

Craig J. Neal,[a] Abinaya Sindu Pugazhendhi,[b] Elisabeth M. Shiffer,[c] Candace R. Fox,[c] Muhammad Hassan Mehmood Kalyar,[c] Elayaraja Kolanthai,[a] Katarzyna Stan-Glowinska,[d] Daniel Brown,[e] Khao Minh Ta,[e] Joanna Wojewoda-Budka,[d] Natalia Sobczak,[d] Marco Molinari,[e] Griffith D. Parks,[c] Melanie J. Coathup[b] and Sudipta Seal *[a,b,c]

With the growing threat of emergent microbes, such as novel viruses and drug-resistant bacteria, more robust and broad-spectrum antimicrobial technologies are of critical importance. Nanomaterials have the potential to deliver broad-spectrum antimicrobial effects while maintaining resistance to degradation in various application environments. In the present study, a multi-metal oxide nanoparticle formulation with substantial antimicrobial activity was developed, outperforming a previous bimetallic composition. The formulation was produced through a variation of an established method wherein the multi-metal oxide is formed through precursor ageing in a peroxide solution environment (room temperature, 8-week ageing period). Silver/zinc-modified cerium oxide nanoparticles exhibited substantial antiviral (0.05 mg mL^{-1} reduced virus titer to beyond detectable ranges for RV14 rhinovirus; ~3 log reduction for vesicular stomatitis virus upon treatment with 0.15 mg mL^{-1} in $TCID_{50}$) and antibacterial (MIC values of ~4, 6, and 6 μg mL^{-1}, respectively, for *P. aeruginosa*, *S. aureus*, and methicillin-resistant *S. aureus* (MRSA)) activities. Of further interest, this nano-formulation evidenced persistent antibacterial activity towards bacterial (*P. aeruginosa* and *S. aureus*) and viral (RV14 rhinovirus; vesicular stomatitis virus, VSV) lab strains resistant to previously developed silver-modified cerium oxide nanoparticles. Nanomaterial characteristics and potential antimicrobial mechanisms were also investigated, with enzyme-mimetic nanozyme generation of reactive oxygen species suggested by density functional theory calculations.

Received 4th December 2025,
Accepted 20th March 2026

DOI: 10.1039/d5nr05105c

rsc.li/nanoscale

1. Introduction

Human infection by pathogenic microbes continues to be a prominent societal issue, with hospital-acquired infections, emergence of novel viral variants, and growth of drug-resistant bacterial strains heightening the general health threat.[1] Central to these issues is the ability of microbes to circumvent or surmount traditional antimicrobial interventions and the inherent difficulties in optimally deploying these methods in certain formats, such as high-touch surfaces in public spaces.[1–3]

The use of nanomaterials has been seen as an attractive approach to address these challenges, given their versatility as functional materials and their greater physicochemical stability over organic antibiotics and antivirals and other conventional antimicrobial materials.[4–9] This stability of inorganic nanomaterials translates to robust activity across temperature ranges and a continuous, sustained activity over technologically relevant time periods (*i.e.*, mechanisms that do not rely on material consumption or irreversible alteration; potential for prolonged systemic dispersion; potential for catalytic reaction mechanisms, *etc.*).[10–12] Among these nanomaterials, metal oxide-based compositions are particularly attractive for biomedical applications because of their stability towards oxidation in biological environments.[13–17]

Cerium oxide is a metal oxide with substantial utility across numerous industrial sectors, largely due to its surface redox chemistry facilitated by the interconversion of cerium sites between Ce^{3+} and Ce^{4+} accompanied by the formation or

[a]*Materials Science & Engineering Department, Advanced Materials Processing and Analysis Center (AMPAC), Nanoscience and Technology Center, University of Central Florida, Orlando, FL, 32816, USA. E-mail: Sudipta.Seal@ucf.edu*
[b]*Biionix Faculty Cluster, College of Medicine, University of Central Florida, Orlando, Florida 32827, USA*
[c]*Burnett School of Biomedical Sciences, College of Medicine, University of Central Florida, Orlando, Florida 32827, USA*
[d]*Institute of Metallurgy and Materials Science, Polish Academy of Sciences, Krakow, 30-418, Poland*
[e]*Department of Physical and Life Sciences, School of Applied Sciences, University of Huddersfield, Huddersfield, HD1 3DH, UK*

healing of oxygen vacancies. In biomedical studies, surface redox reactions of cerium oxide nanoparticles (CNPs) have been identified as mimicking reactions produced by enzymes.[18–20] The class of materials that produce these catalytic reactions is known as nanozymes. These materials, including CNPs, demonstrate the abovementioned stability and thereby show a strong advantage over biological enzymes. Indeed, multiple studies have been published highlighting the utility of pure CNPs, produced by assorted wet chemical synthetic approaches, in antimicrobial applications. Among these studies, smaller particle sizes and surface densities of Ce^{3+} states have been reported as key metrics for the observed activities.[12] The understanding of essential nanomaterial structure–property relationships has progressed such that the production of designer nanomaterials for specific applications, *e.g.*, high-efficacy antimicrobial technologies, is becoming more feasible and practical.[5,21–24]

In many studies, surface redox processes have been coupled with other chemical processes to facilitate catalytic reactions of industrial relevance (*i.e.*, soot reduction by silver-modified cerium oxide surfaces).[25,26] In these reactions, such as the case of nanoscale silver–cerium oxide, interface formation between phases allows for coupling of charge and/or mass transfer processes to produce complex reactions.[27,28] In biomedical applications, similarly structured nanomaterials have been produced to accomplish a larger set of relevant reactions, including antimicrobial compositions. The antimicrobial activity of these materials is often attributed to an increase in reactive oxygen species (ROS) generation and/or the release of metal ions. Therefore, noble and transition metal compositions have been substantially investigated; *e.g.*, Ag/Cu, Au/Pt, Cu/Zn, CuO/Ag, and Ag/ZnO.[9,29–32]

The present work is built on several of our earlier investigations, which demonstrated the use of leaching-stable AgCNP formulations for antiviral and antibacterial applications.[33–35] In these studies, material properties, including particle size, morphology, and chemical state distributions (*i.e.*, cerium redox states, Ce^{3+}/Ce^{4+}; Ag^0, Ag^+), were defined for different silver–cerium oxide nanoparticle formulations and related to virus (rhinovirus, RV14; parainfluenza virus, PIV5; coronaviruses, OC43 and SARS-CoV2) and bacteria (*Pseudomonas aeruginosa*; *Staphylococcus aureus*; methicillin-resistant *S. aureus* (MRSA)) interactions. In the current work, we evaluate the efficacy of a nanomaterial formulation with greater compositional complexity, cerium oxide nanoparticles surface-modified with silver- and zinc-rich phases, as a multi-metal material for antimicrobial applications. In these studies, we hypothesize that inclusion of both transition metals would alter the material's surface redox reaction profile through introduction of additional metal (oxide) domains and/or alteration in silver charge transfer by alloying or complex formation. Initial material characterization and analysis were performed using, primarily, high-resolution transmission electron microscopy, energy-dispersive spectroscopy, and X-ray photoelectron spectroscopy. To facilitate comparison against previously reported silver-modified cerium oxide nanoparticles, studies were performed to assess the material's antiviral/antimicrobial efficacy towards the viruses vesicular stomatitis virus (VSV) and rhinovirus (RV14) and the bacterial species *P. aeruginosa*, *S. aureus*, and methicillin-resistant *S. aureus* (MRSA). The results and analyses from these and related density functional theory-based studies were then used to identify possible mechanisms of the observed substantial antimicrobial activities of the silver/zinc-modified cerium oxide nanoparticle formulation.

2. Materials and methods

2.1 Materials synthesis and characterization

2.1.1 Synthesis. A nanoparticle formulation was produced incorporating silver and zinc with cerium oxide nanoparticles through a one-pot synthesis, similar to a previously reported method.[35] A quiescent aqueous solution of 1.0 mM zinc nitrate (99.5% purity), 1.0 mM silver nitrate (99.9% purity), and 5.0 mM cerium nitrate hexahydrate (99.999% purity) (final molar concentrations) in a borosilicate storage bottle was treated with 2 mL of 3% hydrogen peroxide solution to obtain a final solution volume of 50 mL. The solution was then homogenized using a vortex mixer continuously for 2 minutes, and the bottle's cap was loosened to allow the release of evolved gases. The solution was stored, without perturbation, under dark conditions for up to 8 weeks prior to characterization. All chemical manipulations were performed at standard temperature and pressure. All chemicals were purchased from Sigma Aldrich and were used without further modification.

2.1.2 X-ray photoelectron spectroscopy. Samples were prepared by drying from solution onto clean gold foil substrates inside a chemical fume hood at room temperature. Measurements were performed using an ESCALAB-250 Xi spectrometer with a monochromatic Al-Kα radiation source under a vacuum of $<1 \times 10^{-9}$ mbar, an operating power of 300 W (150 kV, 20 mA), a pass energy of 20 eV, a step size of 0.1 eV, and a spot size of 650 μm. All spectra were referenced to the C–C/C–H binding energy, within the C 1s region, assigned a value of 284.6 eV. Peak assignments were performed based on the reported values in the relevant published literature.

2.1.3 High-resolution transmission electron microscopy. Samples for transmission electron microscopy (TEM) studies were prepared according to the following procedure: a droplet of the aqueous suspension containing nanoparticles was poured onto a copper grid covered with a thin carbon layer and air-dried. Detailed analysis of nanoparticles was performed, including bright-field imaging (BF), selected area diffraction pattern (SADP), high-resolution imaging in TEM (HRTEM) and scanning transmission electron microscopy (STEM) in high-angle annular dark field mode. Mapping of elemental distribution in the selected areas was carried out using a Themis G2 200 Probe Cs-corrected transmission electron microscope, operating at 200 kV and equipped with X-FEG, HAADF-STEM and Super-X EDX systems.

2.1.4 Computational methodology. Spin-polarized density functional theory calculations were performed using the VASP

code.[36–38] The frozen-core projector augmented-wave (PAW) method was utilized with a plane-wave basis set with a cutoff of 500 eV.[39] 3D boundary conditions were implemented. The cut-off energy and *k*-point mesh were checked for convergence, as in our previous calculations. The exchange–correlation functional was the Perdew–Burke–Ernzerhof (PBE) GGA.[40] An effective U = 5 eV was applied to the Ce f orbitals using the Dudarev method[41] to enable localization of Ce^{3+} states as in our previous studies.[42–45] METADISE code was used to generate all models.[46] The conventional 12-atom bulk CeO_2 unit cell was simulated with the electronic and ionic convergence criteria of 1×10^{-5} eV and 1×10^{-3} eV Å^{-1}, respectively, and the Brillouin zone was sampled using a Γ-centered 5 × 5 × 5 *k*-point mesh. The simulated lattice constant (5.498 Å, space group 225) is overestimated as in previous computational studies due to the usage of the PBE + U methodology.[47–53] The CeO_2 surface models were simulated using the slab method, where the top and the bottom of the slab are allowed to relax. The {100}, {110} and {111} surfaces are modelled as $\sqrt{2} \times \sqrt{2}$, a $\sqrt{2} \times 2$ and $\sqrt{2} \times \sqrt{2}$ expansions with 7 (28 CeO_2 units), 7 (28 CeO_2 units) and 5 (20 CeO_2 units) surface layers, respectively. To remove the dipole of the {100} slab, half of the surface oxygen atoms were moved from one side to the other of the slab. A vacuum gap of 15 Å perpendicular to the surface was introduced to minimize the interaction between images. The surfaces were simulated using the electronic and ionic convergence criteria of 1×10^{-5} eV and 1×10^{-2} eV Å^{-1}, respectively, with the Brillouin zone sampled using a Γ-centered 2 × 2 × 1 *k*-point mesh, with the third vector perpendicular to the surface plane. Oxygen vacancies (on the surface and subsurface layers), Zn dopant atoms and adsorbates were introduced symmetrically on both sides. To reduce the exploration of the configurational space for the adsorption of species, only models based on previous studies were used.[33,54] The adsorbate species (*i.e.*, isolated H_2O_2 and O_2 molecules, and an Ag_3 cluster) were geometry-optimized in a cubic cell of side 10 Å at the Γ point with the electronic and ionic convergence criteria of 1×10^{-5} eV and 1×10^{-2} eV Å^{-1}, respectively. The energy of adsorption was calculated as

$$E_{ads} = (E_{surf+adsorbate} - E_{surf} - E_{adsorbate})/2$$

where $E_{surf+adsorbate}$, E_{surf}, and $E_{adsorbate}$ are the energies of the adsorbates adsorbed onto the surface, the bare surface, and the isolated adsorbate, respectively, and 2 accounts for the adsorption of the adsorbates on both sides of the slab.

2.2. Virus studies

2.2.1 Cells and viruses. Cultures of HeLa cells were grown in Dulbecco's modified Eagle's medium (DMEM, Gibco, Thermo Fisher Scientific) supplemented with 10% heat-inactivated fetal calf serum (HI FBS, Gibco, Thermo Fisher Scientific).

Human rhinovirus 14 (RV14, ATCC, catalog number VR-284) was grown in HeLa cells at 33 °C. RV14 stocks were quantified *via* a $TCID_{50}$ assay using confluent HeLa cells, as described previously.[35] Briefly, the virus stock was serially diluted in DMEM containing 10% bovine serum albumin (BSA 7.5% solution, Gibco, Thermo Fisher Scientific) as a carrier protein. Cells were incubated with diluted virus solutions for one hour at 33 °C. The cells were then washed, the medium was replaced with DMEM containing 2% HI FBS, and the cultures were incubated at 33 °C for 3 days. The cells were stained with a crystal violet solution, and $TCID_{50}$ units were quantified using the Spearman & Kärber algorithm as previously described.[55] The Orsay strain of vesicular stomatitis virus (VSV) was grown in Vero cells at 37 °C for 2 days, and VSV stocks were determined *via* the $TCID_{50}$ assay using confluent HeLa cells, as described above.

2.2.2 AgCNP-resistant rhinovirus selection. AgCNP-resistant (AgCNP2 from a previous study,[35] $AgCNP_{ctrl}$ hereafter) RV14 was generated as described previously.[34] Briefly, ~5×10^5 $TCID_{50}$ units of parental RV14 were incubated with 0.1 mg mL^{-1} $AgCNP_{ctrl}$ for 1 h. The reactions were then diluted in DMEM containing 0.38% BSA and used to generate a virus stock in HeLa cells. These cycles of treatment and expansion were repeated for a total of 3 selection rounds at a nanoparticle concentration of 0.1 mg mL^{-1}. The $AgCNP_{ctrl}$ concentration was then adjusted to 0.2, 0.1, and 0.15 mg mL^{-1} for the 4th, 5th, and 6th selection rounds, respectively. After the 6th round, RV14 was harvested and pelleted as described above.

2.2.3 Nanoparticle–virus inactivation assays. Nanoparticles were prepared, and studies in liquid were performed as previously reported.[35] Briefly, nanoparticles were ultrasonicated, diluted in inactivation buffer to the desired concentrations as indicated in the figure legends, and incubated with the virus at room temperature. After the specified incubation times, the remaining infectious virus was quantified using $TCID_{50}$, as described above.

2.2.4 Statistical analyses. Unless otherwise indicated, values are the mean of three independent samples, with error bars representing the standard deviation. Statistical analysis was performed using GraphPad ordinary one-way ANOVA comparing untreated 1 h samples to nanoparticle-treated samples. In all figures, * indicates a p-value of <0.05, ** indicates a p-value of <0.01, and *** indicates a p-value of <0.001.

2.3. Bacterial studies

2.3.1 Bacterial studies: minimum inhibitory concentration (MIC) determination for Ag/Zn-CNPs. The minimum inhibitory concentration (MIC) of Ag/Zn-CNPs was determined in Tris buffer (25 mM Tris/75 mM NaCl; Tris-NaCl) and in Luria–Bertani (LB) broth. The lowest concentration of Ag/Zn-CNPs that inhibits bacterial growth was measured for *P. aeruginosa* ATCC 15442 (Gram negative), *S. aureus* ATCC 6538 (Gram positive), and methicillin-resistant *S. aureus* ATCC 33592 (MRSA) in Tris-NaCl and LB media at pH 7.2. Bacterial inocula were adjusted to 10^8 CFU per mL. Tris-NaCl and LB media inoculated only with 10^8 CFU per mL bacteria were used as controls. MICs were determined by broth dilution using a 96-well flat-bottom microtiter plate. The final Ag/Zn-CNP concentrations of 2, 4, 6, 8, and 10 μg mL^{-1} were prepared in Tris-NaCl medium for all three bacterial strains. In LB medium, the final

concentrations of 10, 20, 30, 40, 50, 60, 70, 80, and 100 μg mL^{-1} were tested for *P. aeruginosa*, while 10, 20, 30, 40, 50, 60, 70, 80, 100, 200, 300, and 400 μg mL^{-1} were tested for *S. aureus* and MRSA. Cultures were incubated at 37 °C with shaking at 210 rpm for 24 h, and changes in optical density at 600 nm were used to assess bacterial growth in LB medium. Gentamicin was included as a study control group.

2.3.2 Time scale study. To carry out a time-course assay, bacterial inocula were adjusted to 10^8 CFU per mL in protein-free, Tris-NaCl medium. The MIC of Ag/Zn-CNPs (4 μg mL^{-1} for *P. aeruginosa* and 6 μg mL^{-1} for *S. aureus* and MRSA) was evaluated in a final volume of 25 mL. Control groups included bacteria with (i) no treatment and (ii) 20 μg mL^{-1} gentamicin. The cultures were then incubated at 37 °C under agitation (210 rpm). 50 μL from each of the treated samples was spread onto LB agar plates, and growth was assessed at 15, 30, 45, 60, and 75 minutes for *P. aeruginosa* and at 60, 120, 180, and 240 minutes for *S. aureus* and MRSA. Colony-forming units (CFU mL^{-1}) were quantified after incubation at 37 °C for 16 h.

2.3.3 Effect of temperature on Ag/Zn-CNP activity. Bacterial inocula were adjusted to 10^8 CFU per mL, and a time-course study was carried out in Tris-NaCl medium. The MIC of Ag/Zn-CNPs (4 μg mL^{-1} for *P. aeruginosa* and 6 μg mL^{-1} for *S. aureus* and MRSA) was evaluated in a final volume of 10 mL. Cultures without Ag/Zn-CNPs served as the control group and all cultures were incubated at 4 °C under agitation at 210 rpm. Aliquots (50 μL) were spread onto LB agar plates, and growth was assessed after 1 and 24 h for *P. aeruginosa*, and after 3 and 24 h for *S. aureus* and MRSA. Colony-forming units (CFU per mL) were quantified following incubation at 37 °C for 16 h.

2.3.4 Resistance-development towards Ag/Zn-CNPs. Approximately 10^8 CFU per mL of *P. aeruginosa* and *S. aureus* were incubated in LB medium at their sublethal (IC_{50}) concentrations of Ag/Zn-CNPs, corresponding to 20 μg mL^{-1} and 200 μg mL^{-1}, respectively. Cultures were grown at 37 °C under agitation at 210 rpm for 2 h. Then, 50 μL of culture was plated onto LB agar and incubated overnight at 37 °C. A single colony from each plate was then reinoculated into LB medium and exposed again to the IC_{50} concentration of Ag/Zn-CNPs. This treatment cycle was repeated eight times. After the 6th and 8th cycles, *P. aeruginosa* and *S. aureus* were tested for resistance development by exposing them to their MIC values of Ag/Zn-CNPs (30 μg mL^{-1} and 400 μg mL^{-1}, respectively) under the culture conditions of 37 °C and 210 rpm for 16 hours. The cultures were consequently plated onto LB agar and examined for resistant colonies.

2.3.5 Bactericidal effect of Ag/Zn-CNPs on resistant strains. The effect of Ag/Zn-CNPs was studied against AgCNP-resistant strains of *P. aeruginosa* and *S. aureus* (laboratory strains). 10^8 CFU per mL of bacteria were treated with increasing concentrations of Ag/Zn-CNPs in Tris-NaCl (10, 20, 30, 40, 50, and 60 μg mL^{-1}) at 37 °C for 24 hours. 50 μL of the tested samples were plated onto LB agar and incubated overnight at 37 °C. Grown colonies were counted and recalculated to the number of CFU per mL.

2.3.6 Effect of Ag/Zn-CNPs on cell metabolic activity in macrophage cells. The cells were maintained in Dulbecco's modified Eagle's medium (DMEM; Thermo Fisher Scientific, USA) supplemented with 10% heat-inactivated fetal bovine serum (FBS; Thermo Fisher Scientific, USA), 1% (v/v) penicillin–streptomycin (P/S; Thermo Fisher Scientific, USA), and 2 mM L-glutamine. Cultures were kept in a humidified incubator at 37 °C with 5% CO_2. Cell metabolic activity was assessed on days 1 and 3 using an MTT assay [3-(4,5-dimethylthiazol-2-yl)-2,5-diphenyltetrazolium bromide] (M2128, Millipore Sigma, USA). RAW 264.7 macrophages were seeded in 96-well plates at a density of 2.5×10^4 cells per well and cultured at 37 °C with or without Ag/Zn-CNPs at concentrations of 4, 6, 30, 100, or 400 μg mL^{-1}. On the designated culture days, 20 μL of 5 mg mL^{-1} MTT solution was added to each well and incubated for 4 h. The supernatant was then carefully removed, and 100 μL of dimethyl sulfoxide (DMSO) was added to dissolve the resulting formazan crystals. Absorbance was measured using a SpectraMax iD3 multimode microplate reader (Molecular Devices, CA, USA).

2.3.7. Statistical analyses. All bacterial experiments were carried out in triplicate. Data are presented as mean ± standard error. Statistical analysis was performed using two-way ANOVA with a *post-hoc* Tukey's test for comparison between groups (GraphPad Prism, v8, USA). p Values <0.05 were considered significant.

3. Results and discussion

3.1 Synthesis of the Ag/Zn-CNP formulation

Silver and zinc surface phase-modified cerium oxide nanoparticles (Ag/Zn-CNPs) were synthesized by treating an aqueous solution of Ag^+, Zn^{2+}, and Ce^{3+} nitrates with hydrogen peroxide, followed by ageing for 8 weeks. During this ageing period, similar to our observations for pure cerium oxide and silver–cerium oxide nanoparticle formulations produced using comparable methods, the solution coloration changed from dark yellow–orange to pale yellow and finally to colorless. This cycling from clear to orange and back to a clear solution has been ascribed to redox cycling of Ce^{3+}/Ce^{4+} and to the formation/degradation of cerium peroxy and oxyhydroxy complexes, as previously reported for pure cerium nitrate–hydrogen peroxide systems. Additionally, precipitate formation was observed, with a spontaneous re-dispersion occurring over the ageing period, which is also observed for comparable pure cerium and cerium–silver nitrate systems. The extended ageing period is ascribed to the slow kinetics of peroxide oxidation of cerium at the low pH of the synthesis (~3.5), and the absence of observable (*i.e.*, *via* black/brown coloration) or measurable (*vida infra*; Fig. 1I) silver oxide is tentatively attributed to the presence of free peroxide ($Ag_2O + H_2O_2 \rightarrow 2Ag + H_2O + O_2$).

3.2 Materials characterization of silver/zinc–cerium oxide nanoparticles

3.2.1 Microscopy and phase composition. TEM observations (Fig. 1) confirmed the presence of small, aggregated

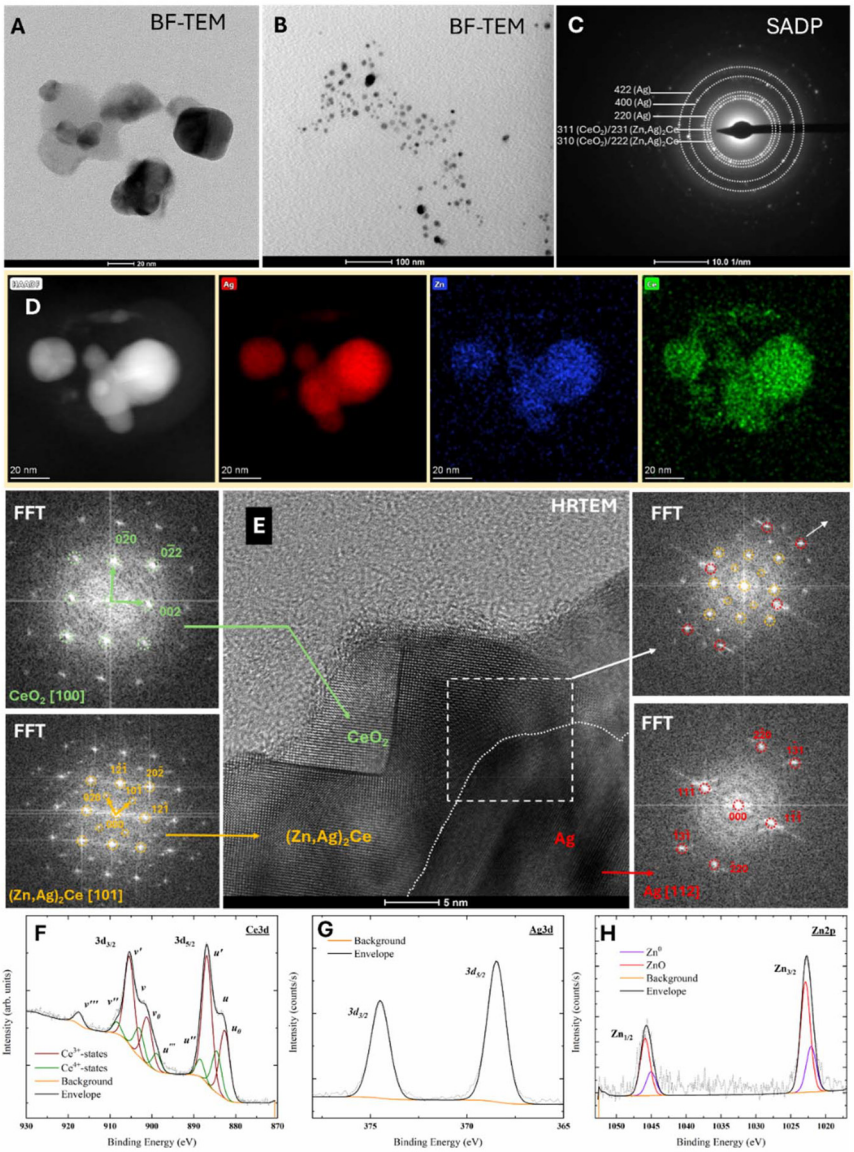

Fig. 1 Materials characterization of silver–zinc cerium oxide nanoparticles. A bright-field transmission electron microscopy (BF-TEM) image taken at higher magnification showing the morphology of some of the observed nanoparticles (A) together with a micrograph recorded at lower magnification (B) showing the distribution of the observed nanoparticles. The selected area diffraction pattern (SADP) obtained from a larger area indicating the presence of different types of nanoparticles (C) together with the scanning transmission electron microscopy high-angle annular dark field (STEM-HAADF) image with the results of elemental mapping indicating intermixing of cerium, silver and zinc in the observed area (D). High-resolution transmission electron microscopy (HRTEM) image with fast Fourier transforms (FFT) from selected regions showing the details of the structure and symmetry of the observed nanoparticles. The *d* values obtained from HRTEM images (E) suggest the formation of Zn-rich compounds. X-ray photoelectron spectroscopy (XPS) measurements with binding energy regions for Ce 3d (F), Ag 3d (G), and Zn 2p (H) chemical states. Peak fittings of Ce^{3+} and Ce^{4+} states provide insight into the density of oxygen vacancies at the material surface and thereby their unique redox chemistry. Interestingly, silver (G) content in the nanoparticle formulation is observed in a metallic state, while zinc (H) occurs in both metallic and oxide states. The range of component valences may also contribute to the observed antimicrobial activity *via* associated redox reactions such as the generation of free radicals by engineered nanoceria formulations.

clusters of spherical-shaped nanoparticles with a mean diameter of 11 nm (Fig. 1A and B). The EDX elemental mapping indicated intermixing of cerium, silver and zinc within them (Fig. 1D). Literature data on the thermodynamic equilibrium in the Ag–Ce–Zn system are very scarce, and, as expected, even less is known regarding the oxide combinations of these metals. However, in the study of Long *et al.* on the thermodynamics of Ag–Ce–Zn, the isothermal cross-sections were calculated and experimentally verified at 450 and 600 °C.[56] It has been shown that Ag_2Ce and Zn_2Ce phases can be combined as $(Ag,Zn)_2Ce$ because of their mutual solubility. The Ag_2Ce phase (Pearson symbol oI12, space group *Imma*) possesses the lattice parameters of a = 0.48 nm, b = 0.709 nm, and c = 0.82 nm,[57] while the Zn_2Ce phase lattice parameters (with the same space

group as Ag_2Ce) are very similar as follows: a = 0.4633 nm, b = 0.7538 nm, and c = 0.749 nm.[58] Therefore, in the electron diffraction pattern obtained from a larger area, beside the presence of silver nanoparticles (AgNPs), the $(Zn,Ag)_2Ce$ phase was also identified (Fig. 1C). Cerium oxide has a cubic structure with the $Fm\bar{3}m$ space group (lattice parameter a = 0.547 nm), where Ce^{4+} is bonded to eight equivalent O_2^- atoms, while O_2^- is bonded to four equivalent Ce^{4+}. On the other hand, silver has the same structure as CeO_2 (cubic with the $Fm\bar{3}m$ space group) with a lower lattice parameter a = 0.41 nm. It is also worth mentioning that silver is able to dissolve relatively high amounts of zinc (up to 20 at%) without changing its structure.[59] During the TEM studies, it was found that Zn-containing particles $(Zn,Ag)_2Ce$ (see an example in Fig. 1E) are not stable under an electron beam, causing difficulties in data acquisition.

Kourouklis *et al.* have studied ceria pressure-induced phase transformation up to 35 GPa, and by recording the Raman spectra, they observed this phenomenon near 31 GPa, when the structure of CeO_2 changed from the above-mentioned fluorite-type to the so-called cotunnite structure ($PbCl_2$ type, orthorhombic, *Pnma*).[60] However, in our case, the phase parameters were fitted to the cubic structure of ceria (Fig. 1C); therefore, both ceria and $(Zn,Ag)_2Ce$ are marked as possible phases. High-resolution transmission electron microscopy (HRTEM) observations evidenced the presence of silver, $(Zn,Ag)_2Ce$ and CeO_2 compounds (Fig. 1E). The structure and symmetry of the observed nanoparticles were confirmed by fast Fourier transforms (FFT) collected from the selected regions, showing ceria NPs of cubic symmetry oriented along the [001] axis, AgNPs along [112] and $(Zn,Ag)_2Ce$ located between them and oriented along the [101] axis. Chemical state analysis was also performed for the particle samples to further assess the formulation's phase composition and provide potential insight into later detailed biomedical properties/behaviors.

3.2.2 Chemical state composition analysis of silver/zinc–cerium oxide nanoparticles. X-ray photoelectron spectroscopy (XPS) was performed (Fig. 1) with analysis focused primarily on the Ce 3d, Ag 3d, and Zn 2p binding energy regions (Fig. 1B, C and D, respectively). Curve fitting was performed for all spectra over the measured signal envelopes using peaks chosen by reference to the relevant literature and database (Thermo Scientific Avantage Data System). The fitted spectra in the Ce 3d region are reflective of the mixed valence state (Ce^{3+}/Ce^{4+}) typically observed for cerium oxide. Peaks attributed to each of the formal oxidation states are presented in Fig. 1G. Semi-quantitative analysis, performed through summation over area-under-the-curve calculations for specific chemical states

$$\%Ce^{3+} = 100 \times \sum \int \{u_0, v_0, u', v'\} / \sum \int \{\text{all fitted peaks}\}$$

where u_0, v_0, u', and v' represent Ce^{3+}-associated states and the calculated percentage is with respect to the total measured population of cerium state-related signal peaks (all fitted peaks), suggests a significant (calculated $\%Ce^{3+}$ = 51.18) population of Ce^{3+}-associated states for the Ag/Zn-CNP formulation. This relatively high percentage of reduced chemical state cerium sites is characteristic of this synthesis: with previous investigations of pure and silver-modified cerium oxide nanoparticle formulations being similarly rich in Ce^{3+} [61–63] For silver-modified cerium oxide materials, Ce^{3+} states have been observed in published experimental studies at higher densities at silver–cerium oxide interfaces, with related theoretical investigations indicating greater stability for silver ions at surface Ce^{3+}-sites. Similar to our previous findings for a silver-modified cerium oxide nanoparticle formulation (previously reported as AgCNP2), the signal in the Ag 3d region is well described by fitting to a metallic silver (Ag^0)-associated doublet (Fig. 1H). Interestingly, the signal envelope peaks in the Zn 2p binding energy region show asymmetry, with fitted doublets related to metallic (Zn^0) and cationic (Zn^{2+}) states approximating the measurement curve (Fig. 1I). The determined chemical state distributions for silver and zinc appear to corroborate findings from HRTEM analysis; specifically, the presence of larger silver nanoparticles and more complex $(Ag,Zn)_2Ce$ compound phases. However, it should also be noted that other studies have identified silver oxide interphase regions directly at silver–ceria interfaces; therefore, we should consider that these XPS measurements do not capture the total chemical state distribution of material components in complete detail. It is possible that oxide states for silver exist in minor populations that are not discernible in our collected XPS spectra, though they may contribute to catalytic behaviors.

We next considered the antimicrobial efficacy of this synthesized Ag/Zn-CNP formulation towards assorted viruses (enveloped vesicular stomatitis virus and non-enveloped RV14 rhinovirus) and bacteria (Gram-positive *S. aureus* and methicillin-resistant *S. aureus*; Gram-negative *P. aeruginosa*) species.

3.3 Virus studies

3.3.1 Silver/zinc cerium oxide nanoparticles display potent antiviral activity against rhinovirus and vesicular stomatitis virus. To determine the extent to which silver-modified CNPs prepared by a comparable synthesis approach and reported previously ($AgCNP_{ctrl}$) and Ag/Zn-CNPs inactivate rhinovirus (RV14) and vesicular stomatitis virus (VSV), aqueous solutions of nanoparticles and virus were incubated together for 1 h. The remaining infectious virus was determined using the 50% tissue culture infectious dose ($TCID_{50}$) assay. Here, we show that Ag/Zn-CNPs inactivate RV14 in a dose-dependent manner, with 0.05 mg mL^{-1} reducing the remaining virus titer to beyond detectable ranges (Fig. 2A). Ag/Zn-CNPs also demonstrate dose-dependent inactivation of VSV (Fig. 2B). However, it is notable that higher concentrations of Ag/Zn-CNPs are necessary to achieve the same log reduction in virus titer for VSV *versus* RV14. Time-course studies showed rapid anti-viral activity of AgZn-CNPs against RV14 (Fig. 2C) and VSV (Fig. 2D), with greater than 50% total virus inactivation occurring within 15 min. The effective concentrations of Ag/Zn-CNPs were used to compare the antiviral activity of Ag/Zn-CNPs *versus* $AgCNP_{ctrl}$. The above finding that Ag/Zn-CNP concentrations of

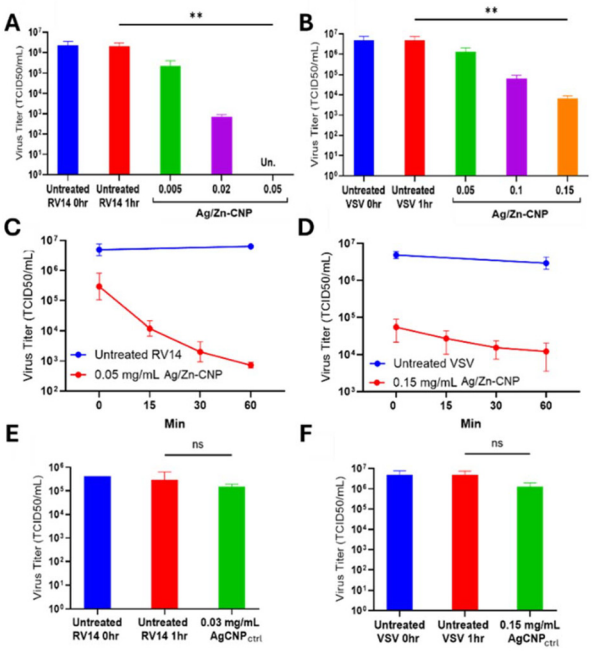

Fig. 2 Effects of 77WC-1 and AgCNP3 nanoparticles on RV14 and VSV infectivity. Liquid reactions of virus and nanoparticles were incubated at room temperature for 1 h. Nanoparticle and virus reactions were collected 1 h post-nanoparticle addition, while untreated virus controls were collected at 0 h and 1 h. The remaining infectious virus titers were determined by the $TCID_{50}$ assay. (A and B) Increasing concentrations of 77WC-1 nanoparticles or buffer alone were incubated with RV14 (A) or VSV (B) and then assayed for the remaining infectious virus. (C and D) 0.05 mg mL^{-1} and 0.15 mg mL^{-1} of 77WC-1 was incubated with RV14 (C) and VSV (D), respectively. Samples were collected at 0, 15, 30, and 60 min, and the $TCID_{50}$ assay was used to quantify infectious virus in each sample. (E and F) AgCNP3 nanoparticles were incubated with RV14 (E) and VSV (F) at concentrations of 0.03 mg mL^{-1} and 0.15 mg mL^{-1}, respectively, for 1 h at room temperature and then collected to quantify infectious viruses. Values in all panels are the mean of three replicates with error bars representing standard deviation.

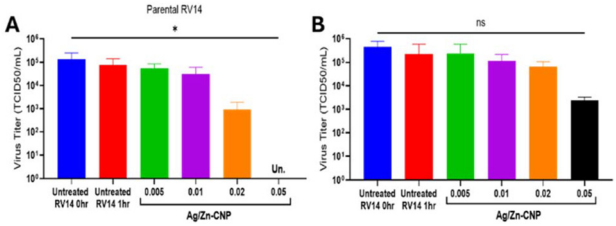

Fig. 3 Antiviral activity of Ag/Zn-CNPs against AgCNP-resistant RV14. AgCNP-resistant RV14 was generated as described previously.[34] Liquid reactions of parental or AgCNP-resistant RV14 and nanoparticles were incubated at room temperature for 1 h. Nanoparticle and virus reactions were collected at 1 h post-nanoparticle addition, while untreated virus controls were collected at 0 h and 1 h. The remaining infectious virus titers were determined using the $TCID_{50}$ assay. (A and B) Increasing concentrations of Ag/Zn-CNPs or buffer alone were incubated with parental RV14 (A) or AgCNP-resistant RV14 (B) and then assayed for the remaining infectious virus. Values in all panels are the mean of three replicates with error bars representing standard deviation.

0.02 mg mL^{-1} and 0.15 mg mL^{-1} reduced >50% infectivity of RV14 and VSV, respectively, contrasts with the results in Fig. 2E and F showing treatment with concentrations of 0.03 mg mL^{-1} and 0.15 mg mL^{-1} of $AgCNP_{ctrl}$ being ineffective at inactivating RV14 and VSV, respectively. Taken together, these data demonstrate that Ag/Zn-CNPs rapidly inactivate RV14 and VSV at lower concentrations than the previous nanoparticle formation $AgCNP_{ctrl}$.

3.3.2 Ag/Zn-CNPs demonstrate antiviral activity against AgCNP-resistant RV14. AgCNP-resistant RV14 was previously generated *via* sequential rounds of exposure to suboptimal AgCNPs and was shown to gain resistance to AgCNP-mediated inactivation.[34] To determine the extent to which Ag/Zn-CNPs can inactivate AgCNP-resistant RV14, aqueous solutions of nanoparticles and virus were incubated together for 1 h. The remaining infectious virus was determined using the 50% tissue culture infectious dose ($TCID_{50}$) assay. Here, we show that Ag/Zn-CNPs inactivate parental RV14 in a dose-dependent manner, with 0.05 mg mL^{-1} reducing the remaining virus titer to beyond detectable ranges (Fig. 3A). Ag/Zn-CNPs also demonstrate dose-dependent inactivation of AgCNP-resistant RV14 (Fig. 3B), with 0.05 mg mL^{-1} resulting in a 2 log reduction in virus titer. Notably, the log reduction in resistant RV14 is considerably lower than that observed for the parental virus, suggesting that AgCNP-resistant RV14 might be partially resistant to Ag/Zn-CNP inactivation. Together, these data demonstrate that Ag/Zn-CNPs display antiviral activity against AgCNP-resistant RV14, although higher doses of nanoparticles might be necessary to inactivate the resistant virus.

3.4 Bacterial studies

3.4.1 Silver/zinc–cerium oxide nanoparticles in the absence of protein. *P. aeruginosa*, *S. aureus*, and MRSA when treated with Ag/Zn-CNPs in a simple 25 mM Tris/75 mM NaCl buffer medium, containing no potentially surface-fouling biomolecules, caused a concentration-dependent reduction in bacterial viability (Fig. 4A–C, respectively). When all three bacterial species were exposed to Ag/Zn-CNPs, it resulted in a significant decrease in CFU per mL compared with the untreated controls, with complete eradication measured at doses >2 μg mL^{-1} for the *P. aeruginosa* group ($p < 0.0001$) and >4 μg mL^{-1} for the *S. aureus* and MRSA groups ($p < 0.0001$). The MIC for *P. aeruginosa* was found to be ~4 μg mL^{-1}, and treatment with 2 μg mL^{-1} resulted in an ~3 log reduction in CFU per mL relative to the control. *S. aureus* showed a similar trend, with an MIC of approximately 6 μg mL^{-1}. Notably, MRSA exhibited the greatest susceptibility to Ag/Zn-CNPs when compared to gentamicin with an MIC of approximately 6 μg mL^{-1}. Even in the presence of gentamicin (20 μg mL^{-1}), only an ~3 log reduction in CFU per mL was observed for MRSA when compared with the untreated group. The results indicate that Ag/Zn-CNPs have a potent bactericidal effect against both Gram-negative and Gram-positive bacteria, including antibiotic-resistant MRSA.

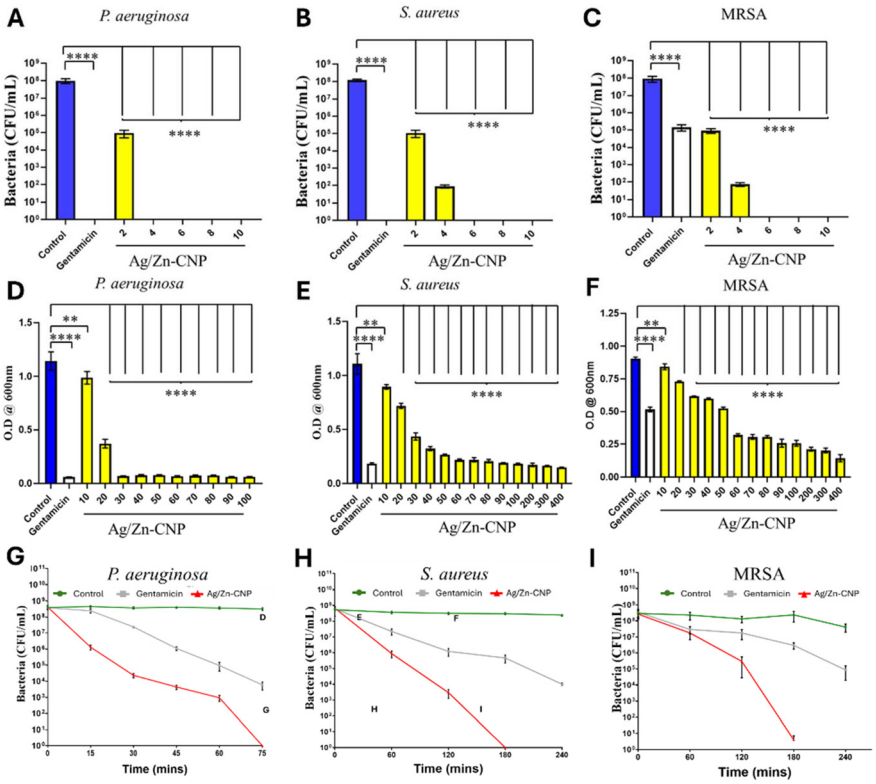

Fig. 4 Bactericidal efficacy of Ag/Zn-CNPs against *P. aeruginosa*, *S. aureus* and MRSA and time-dependent studies. Each bacterial strain was suspended in Tris-NaCl, pH 7.5 and treated with increasing concentrations of Ag/Zn-CNPs and gentamicin (20 μg mL^{-1}) in a 96-well microtiter plate before being incubated for 24 hours at 37 °C (A–C). The MIC values of Ag/Zn-CNPs were found to be 4 μg mL^{-1} for *P. aeruginosa* (A), 6 μg mL^{-1} for *S. aureus* (B), and 6 μg mL^{-1} for MRSA (C). Nanoparticle efficacy towards these strains at ~10^8 CFU per mL was further tested in Luria-Bertani (LB) broth and compared against gentamicin (20 μg mL^{-1}) in a 96-well microtiter plate, followed by incubation at 37 °C for 24 h. The MIC values of Ag/Zn-CNPs were determined to be 30 μg mL^{-1} for *P. aeruginosa* (D) and 400 μg mL^{-1} for *S. aureus* (E) and MRSA (F). Experiments for both sets of studies were carried out in triplicate, and data are presented as mean ± standard error. *p < 0.05, **p < 0.01, ***p < 0.001, and ****p < 0.0001. Growth curves for controls, gentamicin (20 μg mL^{-1}), and Ag/Zn-CNPs at the respective MIC concentrations for each bacteria. When tested at the MIC of Ag/Zn-CNPs, an ~7 log reduction was seen in each group, exceeding the EPA minimum requirement for an antibacterial product.

3.4.2 Silver/zinc–cerium oxide nanoparticles in the presence of protein. The antibacterial efficacy of Ag/Zn-CNPs was investigated against *P. aeruginosa*, *S. aureus*, and MRSA when cultured in protein-rich LB medium (Fig. 4D–F, respectively). A dose-dependent decrease in bacterial growth was observed for all three strains. *P. aeruginosa* growth was significantly reduced at Ag/Zn-CNP concentrations >20 μg mL^{-1} (p < 0.0001). Similarly, *S. aureus* and MRSA growth was significantly reduced at concentrations >10 μg mL^{-1} and >20 μg mL^{-1} (p < 0.05), respectively. However, it is notable that MIC values measured in LB broth were significantly lower than those measured for protein-free buffer medium. It is proposed that this difference is partly ascribable to fouling of the material surface by biomolecule adsorption. Modification of the material surface can alter surface chemistry, including enzyme-mimetic redox reactions shown previously to contribute to antimicrobial performance, as well as function as a physical barrier between the nanoparticle and the environment. The greatest observed efficacy was towards the Gram-negative *P. aeruginosa* viability, with an MIC of around 30 μg mL^{-1}, while MIC values for the Gram-positive *Staphylococcus* strains were markedly higher at ~400 μg mL^{-1}. Interestingly, this trend in Gram-positive *versus* Gram-negative bacteria inactivation was previously observed, for the same bacterial strains, for AgCNPs produced by a comparable synthesis.[33]

3.4.3 Bacterial inactivation kinetics. A time-dependent study of bacterial inactivation by Ag/Zn-CNPs was performed for all three bacterial strains at their respective MIC values (4 μg mL^{-1} for *P. aeruginosa*; 6 μg mL^{-1} for *S. aureus* and MRSA) in Tris-NaCl medium. A progressive and rapid reduction in viable bacteria was observed for all three bacterial species when treated with Ag/Zn-CNPs, whereas the effects of gentamicin occurred at a significantly slower rate for all tested strains (reaching only 4, and 3 log reductions for *P. aeruginosa*, *S. aureus*, and MRSA, respectively, by times of complete inactivation for Ag/Zn-CNPs). For *P. aeruginosa* (Fig. 4G), complete inhibition of bacteria by Ag/Zn-CNPs was observed by 75 minutes, whereas cells treated with gentamicin saw only a 5 log reduction within the same time period. Interestingly, the observed trend of greater sensitivity of *P. aeruginosa* compared to *Staphylococcus* strains occurred in these kinetic studies: with complete bacterial elimination occurring by 180 minutes

(*S. aureus*, Fig. 4H; MRSA, Fig. 4I). Ag/Zn-CNPs demonstrated rapid and potent bactericidal activity across all tested species in Tris-NaCl medium, outperforming gentamicin. To further evaluate Ag/Zn-CNPs' utility as a potent antimicrobial agent, we next examined the potential for a resistant strain to be developed.

3.4.4 Probe of resistance development following repeated-use testing towards Ag/Zn-CNPs. Repeated exposure of *P. aeruginosa* and *S. aureus* to sub-lethal concentrations (IC_{50}) of Ag/Zn-CNPs was performed, and their susceptibilities at the respective, previously determined, MIC values were analyzed. Bacteria were exposed to eight sequential sub-lethal exposure and re-culture cycles, with potential resistance development evaluated by treating sub-cultures at the 6th (Fig. 5A and C) and 8th (Fig. 5B and D) cycles at their respective MIC values in LB medium. Across the studied bacterial species, no substantial increase in tolerance or survival was detected in the presence of Ag/Zn-CNPs (Fig. 5), suggesting no appreciable tendency towards the development of phenotypic resistance, even after multiple cycles of exposure. However, it was found upon performing a similar study that lab strains of AgCNP-resistant *P. aeruginosa* and *S. aureus* could be produced. In a follow-up study, we examined the susceptibility of these AgCNP-resistant strains towards Ag/Zn-CNPs.

3.4.5 Susceptibility of AgCNP-resistant strains to Ag/Zn-CNPs in Tris-NaCl. Upon treatment with Ag/Zn-CNPs, AgCNP-resistant *P. aeruginosa* and *S. aureus* (laboratory) strains experienced dose-dependent decreases in viability. For both bacterial species, the measured MIC values for the parental strains (Fig. 5E and G, ~4 and 6 μg mL^{-1}, for *P. aeruginosa* and *S. aureus*, respectively) were significantly lower ($p < 0.0001$) than those measured for the corresponding AgCNP-resistant strains (Fig. 5F and H, ~50 and 60 μg mL^{-1}, for *P. aeruginosa* and *S. aureus*, respectively), suggesting some increase in bacterial robustness towards Ag/Zn-CNP exposure as well as demonstrating a persistent antimicrobial efficacy of the Ag/Zn-CNP formulation. The overall susceptibility of Gram-negative *Pseudomonas* was slightly lower than that of Gram-positive *Staphylococcus*.

3.5 Antimicrobial function discussion

In our previous studies of AgCNP formulations towards viruses and bacteria, an initial probe into the respective mechanisms of antimicrobial action was performed. Treatment of an enveloped parainfluenza virus (PIV5; a negative-sense, single-stranded RNA virus) with AgCNPs ($AgCNP_{ctrl}$ in the present study) induced an aggregation of virions, suggested by a dose-dependent decrease in hemagglutination of red blood cells by NP-treated PIV5 inocula and by gradient centrifugation studies. Importantly, this observation of NP-induced virus aggregation in centrifugation occurred without appreciable segregation of virions into lower-density gradient bands. This observation allows an important insight: specifically, the dominant mechanism of viral inactivation is likely not protein binding or general surface degradation/modification due to disruption of the integrity of the virus particle, but rather that

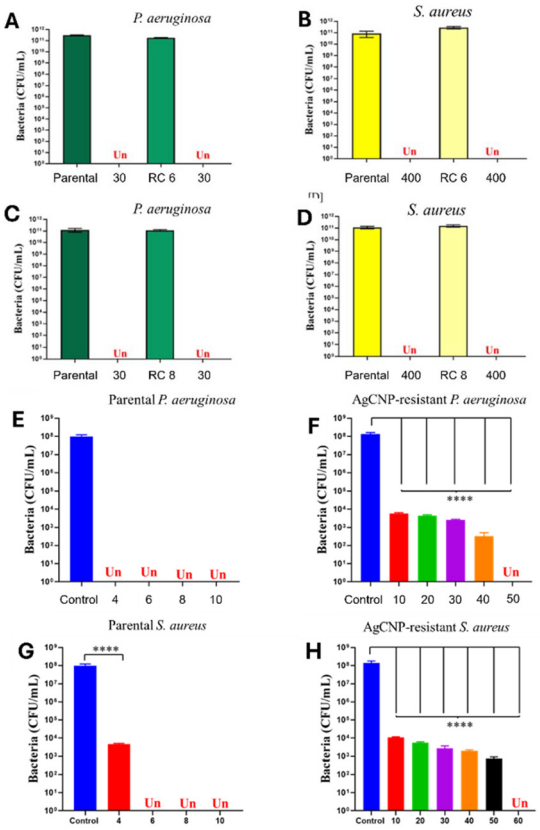

Fig. 5 Resistance development to Ag/Zn-CNPs assessed after repeated exposure rounds in LB medium. (A and C) Parental *P. aeruginosa* and *P. aeruginosa* cells isolated after the 6th (RC 6) and 8th (RC 8) cycles were treated with Ag/Zn-CNPs of 30 μg mL^{-1} (MIC). Cells are not detected (Un) after 24 hours of treatment in both phenotypes. (B and D) Parental *S. aureus* and *S. aureus* cells isolated after the 6th (RC 6) and 8th (RC 8) cycles were treated with Ag/Zn-CNPs of 400 μg mL^{-1} (MIC). Cells are not detected (Un) after 24 hours of treatment in both phenotypes. This demonstrates that when cells were repeatedly exposed to Ag/Zn-CNPs, it did not induce resistance development. Antibacterial activity of Ag/Zn-CNPs against parental and AgCNP resistant *P. aeruginosa* and *S. aureus*. (E and G) Parental *P. aeruginosa* and *S. aureus* strains treated with Ag/Zn-CNPs (4, 6, 8 and 10 μg mL^{-1}). Cells are not detected (Un) after treating them with 4 μg mL^{-1} in *P. aeruginosa* and 6 μg mL^{-1} in *S. aureus*. (F and H) AgCNP resistant *P. aeruginosa* and *S. aureus* treated with Ag/Zn-CNP (10, 20, 30, 40, 50 and, 60 μg mL^{-1}). Cells are not detected (Un) at 50 μg mL^{-1} in *P. aeruginosa* and 60 μg mL^{-1} in *S. aureus*. The results are shown as mean ± standard error, and the experiments were conducted in triplicate. *$p < 0.05$, **$p < 0.01$, ***$p < 0.001$, and ****$p < 0.0001$ (data for the pure and Ag@CeO_2 systems are taken from Pugazhendhi *et al.*[33] and Wei *et al.*[2,3,54]).

the NPs bind virus surface sites and inhibit an early stage of infection. In the same study, a lab strain of non-enveloped rhinovirus (RV14; a single-stranded, positive-sense RNA virus) was produced and was found to be substantially less sensitive to $AgCNP_{ctrl}$ than the parental strain. Genomic analysis identified five point mutations, two of which induced changes in amino acid identity (the other three being silent mutations in the VP3 protein encoding region) and both in a superficial/exterior region of a surface-binding protein subunit (VP1). While these

findings are not direct evidence, the loss of virus inactivation and the presence of amino acid mutations which converted hydrophilic to hydrophobic amino acid expressions implicate these proteins in the virus inhibition mechanism. Our prior work[2] showed that AgCNP-treated viruses had lost receptor binding. It is possible that the ability of Ag/Zn-CNPs to bypass AgCNP resistance reflects (i) prolonged interactions of Ag/Zn-CNPs with virions, (ii) improved access of Ag/Zn-CNPs to the virus receptor-binding domain, or (iii) higher denaturation of viral capsid proteins, leading to increased virus aggregation and/or blocks in uncoating of virus during infection.

The corresponding studies of $AgCNP_{ctrl}$ treatment on bacterial species (*P. aeruginosa*, *S. aureus*, and MRSA) evidence effects from reactive oxygen species (ROS) generation, DNA damage, modulation of cellular oxygen metabolism, and particle adsorption on cell viability.[33] For all tested bacteria, cell lysis was observed. Interestingly, despite the apparent multitude of contributing antibacterial mechanisms, the results of the present study further demonstrate the potential to produce AgCNP-resistant strains of *P. aeruginosa* and of *S. aureus*. Ag/Zn-CNPs retain antibacterial activity towards these strains, suggesting an incomplete overlap in the dominant mechanisms producing the antibacterial outcome. Measurements of antibacterial performance at 4 °C (Fig. S1) reflect a retention of formulating antibacterial activity and suggest that the dominant antibacterial processes are not appreciably rate-controlled or limited by thermal activation, including metabolic processes. Follow-up studies that further probe the observed resistance are underway, though the results from the current study note a more complex phase distribution of formulation components (Fig. 1) which may modify surface interactions between bacterial surface structures and the Ag/Zn-CNPs, and density functional theory (DFT) studies suggest a more favorable generation of ROS relative to AgCNPs.

In the present DFT investigation (Fig. 6 and Table S1), we studied hydrogen peroxide (H_2O_2) and its dissociated products (H/OO/H, H/OOH, and HO/OH) adsorbed on the {111}, {110} and {100} surfaces of cerium dioxide at different surface compositions including stoichiometric pure systems, $Ag@CeO_2$, $Zn@CeO_2$ and $Zn/Ag@CeO_2$, and oxygen deficient pure systems, $Ag@CeO_{2-x(SL)}$, $Zn@CeO_{2-x(SL)}$ and $Zn/Ag@CeO_{2-x(SL)}$, where the oxygen vacancy is positioned in the top layer, and oxygen deficient pure systems, $Ag@CeO_{2-x(SSL)}$, $Zn@CeO_{2-x(SSL)}$ and $Zn/Ag@CeO_{2-x(SSL)}$, where the oxygen vacancy is positioned in the subsurface layer (data for the pure and $Ag@CeO_2$ systems were taken from Pugazhendhi *et al.*[33] and Wei *et al.*[54]). Collectively, the computational results suggest that Ag/Zn-CNPs are more efficient in their generation of antimicrobial ROS and, therefore, potentially better able to induce viral/bacterial inactivation by ROS-mediated pathways, relative to AgCNPs or CNPs alone. The results of the produced calculations, specifically, identify a less negative interaction energy for ROS with Ag/Zn-CNPs; hence, the radicals kill viruses/bacteria more effectively. This relationship can be interpreted as a greater ease for ROS to be released or exchanged with the surrounding environment.

Considering all the models studied for all the three surfaces and the three compositions, in 55% and 69% of the models,

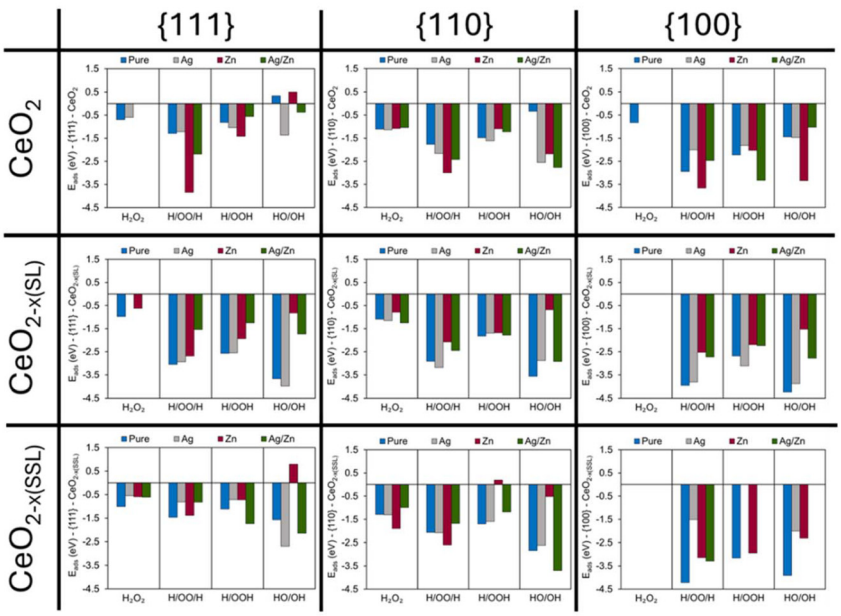

Fig. 6 Density functional theory schematic representation of the adsorption energies (eV). Density functional theory calculations of hydrogen peroxide (H_2O_2) and its dissociated forms (H/OO/H, H/OOH, HO/OH) adsorbed on the {111}, {110} and {100} surfaces of cerium dioxide at different surface compositions including stoichiometric pure, $Ag@CeO_2$, $Zn@CeO_2$ and $Zn/Ag@CeO_2$, and oxygen-deficient pure, $Ag@CeO_{2-x(SL)}$, $Zn@CeO_{2-x(SL)}$ and $Zn/Ag@CeO_{2-x(SL)}$ where the oxygen vacancy is positioned in the top layer, and oxygen deficient pure, $Ag@CeO_{2-x(SSL)}$, $Zn@CeO_{2-x(SSL)}$ and $Zn/Ag@CeO_{2-x(SSL)}$, where the oxygen vacancy is positioned in the subsurface layer. Tabulated data can be found in Table S1.

the adsorption of ROS on Ag/Zn@CeO_2 is less favorable than on Ag@CeO_2 and CeO_2, respectively (Fig. S3 and Table S2). Considering these relationships with respect to specific surface morphologies: (1) in 60%, 50% and 57% of the {111}, {110} and {100} models, respectively, the adsorption of ROS on Ag/Zn@CeO_2 is less favorable than on Ag@CeO_2 and (2) in 60%, 67% and 86% of the {111}, {110} and {100} models, respectively, the adsorption of ROS on Ag/Zn@CeO_2 is less favorable than on CeO_2. Alternatively, the data may be considered with respect to surface composition. From this representation, we find that (1) in 50%, 70% and 44% of the CeO_2, $CeO_{2-x(SL)}$, and $CeO_{2-x(SLL)}$ models, respectively, the adsorption of ROS on Ag/Zn surfaces is less favorable than on the Ag surfaces alone and (2) in 50%, 90% and 67% of the CeO_2, $CeO_{2-x(SL)}$, and $CeO_{2-x(SLL)}$ models, respectively, the adsorption of ROS on Ag/Zn surfaces is less favorable than on the pure surfaces alone. These results indicate that the presence of surface oxygen vacancies (in the $CeO_{2-x(SL)}$ models) drives the inefficiency of the Ag/Zn models compared to Ag and pure (without Ag) models.

Interestingly, despite the pronounced antimicrobial activity and favorable generation of ROS, exposure of a macrophage cell line to Ag/Zn-CNPs (Fig. S2) evidenced a non-toxic character at low concentrations, further supporting their potential use as broad-spectrum antimicrobial agents. While the current study was designed to evaluate efficacy in disinfection, the calculation of therapeutic index (TI) values from bacterial studies marks a first step in assessing material efficacy as a nanopharmaceutical (Fig. S4). Initial measurements in the absence of biomolecules identified TI values of 2.87, 1.91, and 1.91 for *P. aeruginosa*, *S. aureus*, and MRSA, respectively. Similarly, TI values for RV14 and VSV were calculated as approximately 0.574 and 0.077, respectively. The data suggest a potential need for nanoparticle surface modification or engineering before use as a pharmaceutical. Follow-up studies of nanomaterial suitability and design for pharmaceutical applications will consider the antimicrobial efficacy of similar formulations in biological systems, with biological data and metrics such as TI, utilized for the design and optimization of nanomaterial formulations.

4. Conclusions

In the present study, a multi-metal oxide nanoparticle formulation was produced containing zinc and silver-rich surface phases on cerium oxide nanoparticles (Ag/Zn-CNPs). Materials characterization and analyses noted a high relative proportion of cerium sites in a Ce^{3+} formal redox state, predominant metallic state for silver, and the presence of zinc in both cationic Zn^{2+} and metallic Zn^0 states, as evident from XPS measurements. High-resolution transmission electron microscopy imaging and energy-dispersive spectroscopy evidence a complex phase distribution, with elemental mapping and fast Fourier transform crystal pattern analyses suggesting the presence of CeO_2, Ag^0, and potentially $(Ag,Zn)_2$ phases. Treatment of bacterial species (*P. aeruginosa*, *S. aureus*, and MRSA) and viruses (RV14 rhinovirus and VSV) demonstrated a significant antimicrobial activity relative to a previously reported silver-modified cerium oxide nanoparticle formulation (AgCNPs). Furthermore, Ag/Zn-CNPs were found to retain antimicrobial activity towards *P. aeruginosa*, *S. aureus* strains, and RV14 lab strains which are insensitive to AgCNP treatment: further suggesting their improved utility for broad-spectrum antimicrobial technologies. Density functional theory calculations (considering the presence/absence of Ce^{3+}-associated oxygen vacancies and assorted high atomic density surface facets) similarly suggest a greater ability to generate antimicrobial reactive oxygen species, relative to pure pristine or non-stoichiometric cerium oxide or silver-modified cerium oxide surfaces. When the antibacterial efficacy of Ag/Zn-CNPs was compared with our previously published AgCNP activity,[1] the data showed that, in the absence of biomolecules, the MIC of Ag/Zn-CNPs delivered superior activity towards Gram-negative *P. aeruginosa* (4 μg mL^{-1}) as well as to Gram-positive *S. aureus* and MRSA (both 6 μg mL^{-1}) when compared with AgCNPs (20 μg mL^{-1} (*P. aeruginosa*) and 50 μg mL^{-1} (*S. aureus* and MRSA, unpublished data)). Notably, in the presence of media containing biomolecules (*i.e.*, biofouling), the MIC of Ag/Zn-CNPs was found to be lower and thus more potent (30 μg mL^{-1}) when compared to AgCNPs (100 μg mL^{-1}). However, Ag/Zn-CNPs were marginally less potent to *S. aureus* and MRSA (400 μg mL^{-1}) when compared to AgCNPs (300 μg mL^{-1}). Nevertheless, and critically, the present study reveals that Ag/Zn-CNPs effectively eradicated Ag-resistant *P. aeruginosa* and *S. aureus* strains. Furthermore, given that bacterial antimicrobial resistance is considered a severe and global public health crisis, the data confirm remarkably that resistant strains of *P. aeruginosa* and *S. aureus* could not be created after eight sequential sub-lethal exposure and re-culture cycles to Ag/Zn-CNPs.

Author contributions

Craig J. Neal: conceptualization, data curation, formal analysis, investigation, methodology, project administration, and writing – original draft; Abinaya Sindu Pugazhendhi: formal analysis, investigation, methodology, data curation, and writing – original draft; Elisabeth M. Shiffer: formal analysis, investigation, methodology, data curation, and writing – original draft; Candace R. Fox: formal analysis, investigation, methodology, data curation, and writing – original draft; Muhammad Hassan Mehmood Kalyar: formal analysis, investigation, methodology, data curation, and writing – original draft; Elayaraja Kolanthai: formal analysis, investigation, methodology, data curation, and writing – original draft; Katarzyna Stan-Glowinska: formal analysis, investigation, methodology, data curation, and writing – original draft. Daniel Brown, Khao Minh Ta, Joanna Wojewoda-Budka, Natalia Sobczak, Marco Molinari, and Griffith D. Parks: methodology, resources, supervision, and writing – review & editing; Melanie J. Coathup:

methodology, resources, supervision, and writing – review & editing; and Sudipta Seal: conceptualization, supervision, resources, and writing – review & editing.

Conflicts of interest

There are no conflicts of interest to declare.

Data availability

The datasets supporting the findings of this study are available within the article and its supplementary information (SI). Supplementary information: Fig. S1–S3, Tables S1 and S2. See DOI: https://doi.org/10.1039/d5nr05105c.

Acknowledgements

Some of the TEM examination of nanoparticles was financially supported by the Institute of Metallurgy and Materials Science of the Polish Academy of Sciences within the statutory work "Modern copper composite coatings with cerium oxide particles" Z-5/2025 and the MOU between the University of Central Florida Board of Trustees and the Institute of Metallurgy and Materials Science, Polish Academy of Sciences. MM acknowledges the Vice Chancellor's Scholarship Scheme for funding KMT. Calculations were performed using the Orion computing facility and the HPC Violeta at the University of Huddersfield, and the ARCHER2 UK National Supercomputing Service *via* our membership of the UK HEC Materials Chemistry Consortium (MCC; EPSRC EP/X035859/1). SS acknowledges the NSF MRI XPS ECCS: 1726636 grant, allowing XPS measurements at the UCF Materials Characterization Facility.

References

1 C. Tong, H. Hu, G. Chen, Z. Li, A. Li and J. Zhang, Disinfectant resistance in bacteria: Mechanisms, spread, and resolution strategies, *Environ. Res.*, 2021, **195**, 110897.
2 K. R. Wigginton and T. Kohn, Virus disinfection mechanisms: the role of virus composition, structure, and function, *Curr. Opin. Virol.*, 2012, **2**(1), 84–89.
3 H. F. Van Dijk and H. A. Verbrugh, Resisting disinfectants, *Commun. Med.*, 2022, **2**(1), 6.
4 E. Kolanthai, C. J. Neal, U. Kumar, Y. Fu and S. Seal, Antiviral nanopharmaceuticals: Engineered surface interactions and virus–selective activity, *Wiley Interdiscip. Rev.: Nanomed. Nanobiotechnol.*, 2022, **14**(5), e1823.
5 B. Le Ouay and F. Stellacci, Antibacterial activity of silver nanoparticles: A surface science insight, *Nano Today*, 2015, **10**(3), 339–354.
6 C. Weiss, M. Carriere, L. Fusco, I. Capua, J. A. Regla-Nava, M. Pasquali, *et al.*, Toward nanotechnology-enabled approaches against the COVID-19 pandemic, *ACS Nano*, 2020, **14**(6), 6383–6406.
7 A. N. Zelikin and F. Stellacci, Broad–spectrum antiviral agents based on multivalent inhibitors of viral infectivity, *Adv. Healthcare Mater.*, 2021, **10**(6), 2001433.
8 A. Ivask, A. ElBadawy, C. Kaweeteerawat, D. Boren, H. Fischer, Z. Ji, *et al.*, Toxicity mechanisms in Escherichia coli vary for silver nanoparticles and differ from ionic silver, *ACS Nano*, 2014, **8**(1), 374–386.
9 G. Vasiliev, A.-L. Kubo, H. Vija, A. Kahru, D. Bondar, Y. Karpichev, *et al.*, Synergistic antibacterial effect of copper and silver nanoparticles and their mechanism of action, *Sci. Rep.*, 2023, **13**(1), 9202.
10 V. Cagno, P. Andreozzi, M. D'Alicarnasso, P. Jacob Silva, M. Mueller, M. Galloux, *et al.*, Broad-spectrum non-toxic antiviral nanoparticles with a virucidal inhibition mechanism, *Nat. Mater.*, 2018, **17**(2), 195–203.
11 B. Punz, C. Christ, A. Waldl, S. Li, Y. Liu, L. Johnson, *et al.*, Nano-scaled advanced materials for antimicrobial applications–mechanistic insight, functional performance measures, and potential towards sustainability and circularity, *Environ. Sci.:Nano*, 2025, **12**(3), 1710–1739.
12 V. Lozovski, V. Lysenko, V. Piatnytsia, O. Scherbakov, N. Zholobak and M. Spivak, Physical point of view for antiviral effect caused by the interaction between the viruses and nanoparticles, *J. Bionanosci.*, 2012, **6**(2), 109–112.
13 N. M. Zholobak, V. K. Ivanov and A. B. Shcherbakov, *Interaction of nanoceria with microorganisms*, Nanobiomaterials in antimicrobial therapy: Elsevier, 2016, 419–450.
14 L. Babenko, N. Zholobak, A. Shcherbakov, S. Voychuk, L. Lazarenko and M. Y. Spivak, Antibacterial activity of cerium colloids against opportunistic microorganisms in vitro, *Microbiol. J.*, 2012, **74**(3), 54–62.
15 N. Zholobak, Z. Olevinskaia, A. Shcherbakov, V. Ivanov and A. Usatenko, Antiviral effect of cerium dioxide nanoparticles stabilized by low-molecular polyacrylic acid, *J. Microbiol.*, 2010, **72**(3), 42–47.
16 N. Zholobak, A. Shcherbakov, V. Ivanov, Z. Olevinskaya and N. Spivak, Antiviral effectivity of ceria colloid solutions, *Antiviral Res.*, 2011, **90**(2), A67.
17 A. Nefedova, K. Rausalu, E. Zusinaite, A. Vanetsev, M. Rosenberg, K. Koppel, *et al.*, Antiviral efficacy of cerium oxide nanoparticles, *Sci. Rep.*, 2022, **12**(1), 18746.
18 E. G. Heckert, A. S. Karakoti, S. Seal and W. T. Self, The role of cerium redox state in the SOD mimetic activity of nanoceria, *Biomaterials*, 2008, **29**(18), 2705–2709.
19 V. Baldim, F. Bedioui, N. Mignet, I. Margaill and J.-F. Berret, The enzyme-like catalytic activity of cerium oxide nanoparticles and its dependency on Ce 3 + surface area concentration, *Nanoscale*, 2018, **10**(15), 6971–6980.
20 T. Pirmohamed, J. M. Dowding, S. Singh, B. Wasserman, E. Heckert, A. S. Karakoti, *et al.*, Nanoceria exhibit redox state-dependent catalase mimetic activity, *Chem. Commun.*, 2010, **46**(16), 2736–2738.

21 S. Seal, A. Jeyaranjan, C. J. Neal, U. Kumar, T. S. Sakthivel and D. C. Sayle, Engineered defects in cerium oxides: tuning chemical reactivity for biomedical, environmental, & energy applications, *Nanoscale*, 2020, **12**(13), 6879–6899.
22 A. Verma and F. Stellacci, Effect of surface properties on nanoparticle–cell interactions, *Small*, 2010, **6**(1), 12–21.
23 S. Keshavan, P. Calligari, L. Stella, L. Fusco, L. G. Delogu and B. Fadeel, Nano-bio interactions: a neutrophil-centric view, *Cell Death Dis.*, 2019, **10**(8), 569.
24 S. Agarwal, L. Lefferts and B. L. Mojet, Ceria nanocatalysts: shape dependent reactivity and formation of OH, *ChemCatChem*, 2013, **5**(2), 479–489.
25 E. Aneggi, J. Llorca, C. de Leitenburg, G. Dolcetti and A. Trovarelli, Soot combustion over silver-supported catalysts, *Appl. Catal., B*, 2009, **91**(1–2), 489–498.
26 T. Kayama, K. Yamazaki and H. Shinjoh, Nanostructured ceria– silver synthesized in a one-pot redox reaction catalyzes carbon oxidation, *J. Am. Chem. Soc.*, 2010, **132**(38), 13154–13155.
27 G. Preda and G. Pacchioni, Formation of oxygen active species in Ag-modified CeO_2 catalyst for soot oxidation: A DFT study, *Catal. Today*, 2011, **177**(1), 31–38.
28 T. Mitsudome, Y. Mikami, M. Matoba, T. Mizugaki, K. Jitsukawa and K. Kaneda, Design of a silver–cerium dioxide core–shell nanocomposite catalyst for chemoselective reduction reactions, *Angew. Chem., Int. Ed.*, 2012, **51**(1), 136–139.
29 J. Al-Haddad, F. Alzaabi, P. Pal, K. Rambabu and F. Banat, Green synthesis of bimetallic copper–silver nanoparticles and their application in catalytic and antibacterial activities, *Clean Technol. Environ. Policy*, 2020, **22**(1), 269–277.
30 D. M. D. Formaggio, X. A. de Oliveira Neto, L. D. A. Rodrigues, V. M. de Andrade, B. C. Nunes, M. Lopes-Ferreira, *et al.*, In vivo toxicity and antimicrobial activity of AuPt bimetallic nanoparticles, *J. Nanopart. Res.*, 2019, **21**(11), 244.
31 R. Merugu, R. Gothalwal, P. K. Deshpande, D. Mandal, S. Padala, G. Chitturi and K. L, Synthesis of Ag/Cu and Cu/Zn bimetallic nanoparticles using toddy palm: Investigations of their antitumor, antioxidant and antibacterial activities, *Mater. Today Proc.*, 2021, **44**, 99–105.
32 G. R. Andrade, C. C. Nascimento, Z. M. Lima, E. Teixeira-Neto, L. P. Costa and I. F. Gimenez, Star-shaped ZnO/Ag hybrid nanostructures for enhanced photocatalysis and antibacterial activity, *Appl. Surf. Sci.*, 2017, **399**, 573–582.
33 A. S. Pugazhendhi, C. J. Neal, K. M. Ta, M. Molinari, U. Kumar, F. Wei, *et al.*, A neoteric antibacterial ceria-silver nanozyme for abiotic surfaces, *Biomaterials*, 2024, **307**, 122527.
34 C. R. Fox, K. Kedarinath, C. J. Neal, J. Sheiber, E. Kolanthai, U. Kumar, *et al.*, Broad-spectrum, potent, and durable ceria nanoparticles inactivate RNA virus infectivity by targeting virion surfaces and disrupting virus–receptor interactions, *Molecules*, 2023, **28**(13), 5190.
35 C. J. Neal, C. R. Fox, T. S. Sakthivel, U. Kumar, Y. Fu, C. Drake, *et al.*, Metal-mediated nanoscale cerium oxide inactivates human coronavirus and rhinovirus by surface disruption, *ACS Nano*, 2021, **15**(9), 14544–14556.
36 G. Kresse and J. Furthmüller, Efficient iterative schemes for ab initio total-energy calculations using a plane-wave basis set, *Phys. Rev. B:Condens. Matter Mater. Phys.*, 1996, **54**(16), 11169.
37 G. Kresse and J. Hafner, Ab initio molecular-dynamics simulation of the liquid-metal–amorphous-semiconductor transition in germanium, *Phys. Rev. B:Condens. Matter Mater. Phys.*, 1994, **49**(20), 14251.
38 G. Kresse and D. Joubert, From ultrasoft pseudopotentials to the projector augmented-wave method, *Phys. Rev. B: Condens. Matter Mater. Phys.*, 1999, **59**(3), 1758.
39 P. E. Blöchl, Projector augmented-wave method, *Phys. Rev. B:Condens. Matter Mater. Phys.*, 1994, **50**(24), 17953.
40 J. P. Perdew, K. Burke and M. Ernzerhof, Generalized gradient approximation made simple, *Phys. Rev. Lett.*, 1996, **77**(18), 3865.
41 S. L. Dudarev, G. A. Botton, S. Y. Savrasov, C. Humphreys and A. P. Sutton, Electron-energy-loss spectra and the structural stability of nickel oxide: An LSDA+ U study, *Phys. Rev. B:Condens. Matter Mater. Phys.*, 1998, **57**(3), 1505.
42 K. M. Ta, C. J. Neal, M. Coathup, S. Seal, L. J. Gillie, D. J. Cooke, S. C. Parker and M. Molinari, The Buffering Activity of Ceria toward Reactive Oxygen Species: A Density Functional Theory Perspective, *J. Phys. Chem. C*, 2025, **129**(26), 11989–12005.
43 M. Molinari, S. C. Parker, D. C. Sayle and M. S. Islam, Water adsorption and its effect on the stability of low index stoichiometric and reduced surfaces of ceria, *J. Phys. Chem. C*, 2012, **116**(12), 7073–7082.
44 S. Munir, T. Smith, K. M. Ta, L. J. Gillie, D. J. Cooke and M. Molinari, Modelling hydrogen peroxide adsorption on cerium dioxide: the effect of surface strain, *Catal. Sci. Technol.*, 2025, **15**(17), 5150–5166.
45 S. Munir, K. M. Ta, T. Smith, L. J. Gillie, D. J. Cooke, S. C. Parker, *et al.*, Strain Effects on the Adsorption of Water on Cerium Dioxide Surfaces and Nanoparticles: A Modeling Outlook, *J. Phys. Chem. C*, 2024, **128**(43), 18451–18464.
46 G. W. Watson, E. T. Kelsey, N. H. de Leeuw, D. J. Harris and S. C. Parker, Atomistic simulation of dislocations, surfaces and interfaces in MgO, *J. Chem. Soc., Faraday Trans.*, 1996, **92**(3), 433–438.
47 C. Brambila, D. Sayle, M. Molinari, J. Nutter, J. Flitcroft, T. Sayle, *et al.*, Tomographic study of mesopore formation in ceria nanorods, *J. Phys. Chem. C*, 2021, **125**(18), 10077–10089.
48 M. Molinari, A. R. Symington, D. C. Sayle, T. S. Sakthivel, S. Seal and S. C. Parker, Computer-aided design of nanoceria structures as enzyme mimetic agents: The role of bodily electrolytes on maximizing their activity, *ACS Appl. Bio Mater.*, 2019, **2**(3), 1098–1106.
49 S. Moxon, A. R. Symington, J. St, J. M. Flitcroft, J. M. Skelton, L. J. Gillie, D. J. Cooke, S. C. Parker and M. Molinari, Composition-dependent morphologies of

CeO_2 nanoparticles in the presence of Co-adsorbed H_2O and CO_2: a density functional theory study, *Nanoscale*, 2024, **16**(23), 11232–11249.

50 A. R. Symington, R. M. Harker, M. T. Storr, M. Molinari and S. C. Parker, Thermodynamic evolution of cerium oxide nanoparticle morphology using carbon dioxide, *J. Phys. Chem. C*, 2020, **124**(42), 23210–23220.

51 A. R. Symington, M. Molinari, S. Moxon, J. M. Flitcroft, D. C. Sayle and S. C. Parker, Strongly bound surface water affects the shape evolution of cerium oxide nanoparticles, *J. Phys. Chem. C*, 2020, **124**(6), 3577–3588.

52 K. M. Ta, D. J. Cooke, L. J. Gillie, S. C. Parker, S. Seal, P. B. Wilson, R. M. Phillips, J. M. Skelton and M. Molinari, Infrared and Raman diagnostic modeling of phosphate adsorption on ceria nanoparticles, *J. Phys. Chem. C*, 2023, **127**(40), 20183–20193.

53 K. M. Ta, D. O. Wisdom, L. J. Gillie, D. J. Cooke, R. Zhu, M. A. Gonçalves, S. C. Parker, M. Molinari, *et al.*, Sorption of arsenate on cerium oxide: a simulated infrared and Raman spectroscopic identification, *Environ. Sci.*, 2025, **12**(3), 1896–1907.

54 F. Wei, C. J. Neal, T. S. Sakthivel, Y. Fu, M. Omer, A. Adhikary, *et al.*, A novel approach for the prevention of ionizing radiation-induced bone loss using a designer multifunctional cerium oxide nanozyme, *Bioact. Mater.*, 2023, **21**, 547–565.

55 J. Hierholzer and R. Killington, *Virus isolation and quantitation*, Virology methods manual: Elsevier, 1996, pp. 25–46.

56 Z. Long, L. Kang, F. Yin, Z. Li, M. Zhao, Y. Liu, *et al.*, Phase equilibria of the Ag–Zn–Ce (0–33.3 at% Ce) system at 450° C and 600° C, *J. Alloys Compd.*, 2015, **618**, 172–181.

57 K. Gschneidner and F. Calderwood, The Ag-Ce (Silver-Cerium) system, *Bull. Alloy Phase Diagrams*, 1985, **6**(5), 439–443.

58 P. Chiotti and J. Mason, Phase relations and thermodynamic properties for the cerium-zinc systems, *Trans. Soc. Min. Eng. AIME*, 1965, 233.

59 T. Gomez-Acebo, Thermodynamic assessment of the Ag-Zn system, *Calphad*, 1998, **22**(2), 203–220.

60 G. Kourouklis, A. Jayaraman and G. Espinosa, High-pressure Raman study of CeO 2 to 35 GPa and pressure-induced phase transformation from the fluorite structure, *Phys. Rev. B:Condens. Matter Mater. Phys.*, 1988, **37**(8), 4250.

61 S. V. Kuchibhatla, A. S. Karakoti, D. R. Baer, S. Samudrala, M. H. Engelhard, J. E. Amonette, *et al.*, Influence of aging and environment on nanoparticle chemistry: implication to confinement effects in nanoceria, *J. Phys. Chem. C*, 2012, **116**(26), 14108–14114.

62 C. Korsvik, S. Patil, S. Seal and W. T. Self, Superoxide dismutase mimetic properties exhibited by vacancy engineered ceria nanoparticles, *Chem. Commun.*, 2007, (10), 1056–1058.

63 C. J. Neal, T. S. Sakthivel, Y. Fu and S. Seal, Aging of nanoscale cerium oxide in a peroxide environment: Its influence on the redox, surface, and dispersion character, *J. Phys. Chem. C*, 2021, **125**(49), 27323–27334.

